The Phantom Laboratory + imageOwl

Magphan® RT

Precision QA for MR

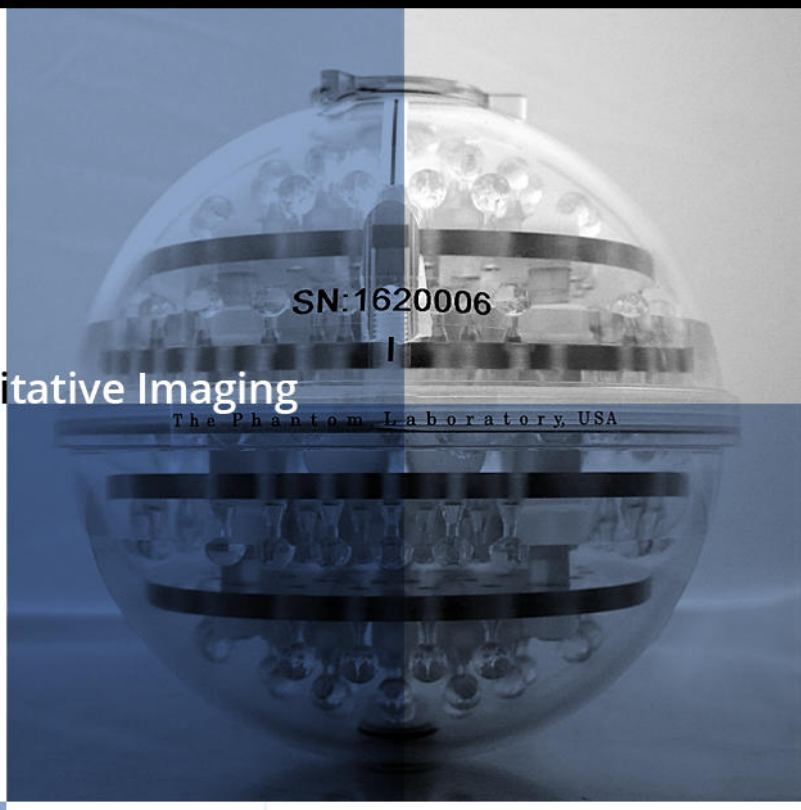

MR QA for Radiotherapy and Quantitative Imaging

Magphan® head and body phantoms address the needs for precise measurements of quantitative MR. The phantoms are supplied with two years of Image Owl's high-powered automated analysis.

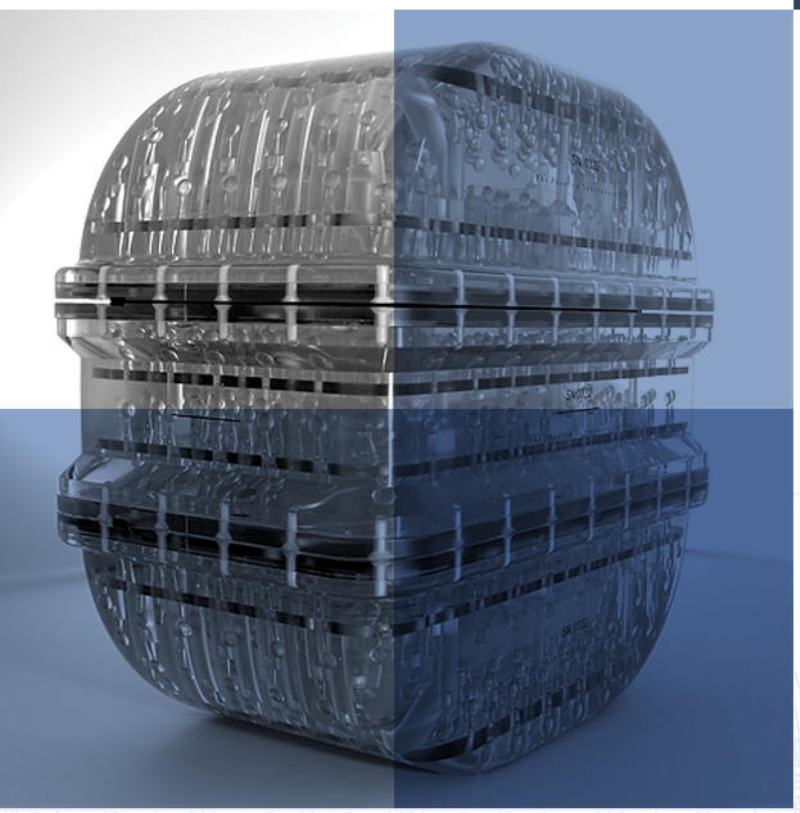

In addition to accurate sub-millimeter distortion measurements, Magphan phantoms include tests for high resolution, slice geometry, noise, uniformity and more. Because it is critical to test the actual image parameters you are using, the phantom is designed to work with a wide range of clinical protocols.

Contact us today for a demo and discussion of your MR QA requirements.

info@phantomlab.com
518-692-1190

Accepted Article

Article Type: Research Article

Quantification of body-torso-wide tissue composition on low-dose CT images via Automatic Anatomy Recognition

[1,2,3]Tiange Liu, [2]Jayaram K. Udupa, [3]Qiguang Miao, [2]Yubing Tong, [2]Drew A. Torigian

[1]School of Information Science and Engineering,

Yanshan University, Qinhuangdao, Hebei, 066004, China

[2]Medical image Processing Group

Department of Radiology

University of Pennsylvania

Philadelphia 19104

US

[3]Xidian University, Xi'an, Shaanxi, 710126, China

Address for correspondence:

Jayaram K. Udupa, PhD

Medical Image Processing Group

Department of Radiology

3710 Hamilton Walk, Goddard Building, 6th floor

Philadelphia PA 19104

jay@mail.med.upenn.edu

This article has been accepted for publication and undergone full peer review but has not been through the copyediting, typesetting, pagination and proofreading process, which may lead to differences between this version and the Version of Record. Please cite this article as doi: 10.1002/mp.13373

This article is protected by copyright. All rights reserved.

Accepted Article

Abstract

Purpose: Quantification of body composition plays an important role in many clinical and research applications. Radiologic imaging techniques such as Dual-energy X-ray absorptiometry (DXA), magnetic resonance imaging (MRI), and computed tomography (CT) imaging make accurate quantification of the body composition possible. However, most current imaging based methods need human interaction to quantify multiple tissues. When dealing with whole-body images of many subjects, interactive methods become impractical. This paper presents an automated, efficient, accurate, and practical body composition quantification method for low-dose CT images.

Method: Our method, named automatic anatomy recognition body composition analysis (AAR-BCA), aims to quantify four tissue components in body torso (BT) – subcutaneous adipose tissue (SAT), visceral adipose tissue (VAT), bone tissue, and muscle tissue – from CT images of given whole-body positron emission tomography/computed tomography (PET/CT) acquisitions. AAR-BCA consists of three key steps – modeling BT with its ensemble of key objects from a population of patient images, recognition or localization of these objects in a given patient image *I*, and delineation and quantification of the four tissue components in *I* guided by the recognized objects. In the first step, from a given set of patient images and the associated delineated objects, a fuzzy anatomy model of the key object ensemble, including anatomic organs, tissue regions, and tissue interfaces, is built where the objects are organized in a hierarchical order. The second step involves recognizing, or finding roughly the location of, each object in any given whole-body image *I* of a patient following the object hierarchy and guided by the built model. The third step makes use of this fuzzy localization information of the objects and the intensity distributions of the four tissue components, already learned and encoded in the model, to optimally delineate in a fuzzy manner and quantify these components. All parameters in our method are determined from training data sets.

This article is protected by copyright. All rights reserved.

Results: 38 low-dose CT images from different subjects are tested in a 5-fold cross validation strategy for evaluating AAR-BCA with a 23-15 train-test data set division. For BT, over all objects, AAR-BCA achieves a false positive volume fraction (FPVF) of 3.7% and false negative volume fraction (FNVF) of 3.8%. Notably, SAT achieves both a FPVF and FNVF under 3%. For bone tissue, it achieves a FPVF and a FNVF both under 3.5%. For VAT tissue, the FNVF of 4.8% is higher than for other objects and so also for muscle (4.7%). The level of accuracy for the four tissue components in individual body sub-regions mostly remains at the same level as for BT. The processing time required per patient image is under a minute.

Conclusions: Motivated by applications in cancer and systemic diseases, our goal in this paper was to seek a practical method for body composition quantification which is automated, accurate, and efficient, and works on BT in low-dose CT. The proposed AAR-BCA method towards this goal can quantify four tissue components including SAT, VAT, bone tissue, and muscle tissue in the body torso with under 5% overall error. All needed parameters can be automatically estimated from the training data sets.

Keywords

Body composition analysis, image segmentation, automatic anatomy recognition (AAR), computed tomography (CT), PET/CT, quantitative imaging.

1. Introduction

1.1 Background

Assessment of body composition is important for various clinical and research applications including evaluation of the effects of obesity upon comorbid disease development, prognosis, and treatment outcome[1-8], and assessment of gender-based or age-based differences of body composition in health and disease[9]. An efficient and accurate technique for quantification of

This article is protected by copyright. All rights reserved.

Accepted Article

body tissue components including subcutaneous adipose tissue (SAT), visceral adipose tissue (VAT), muscle tissue, and bone tissue is needed to perform such assessments practically. With accurate quantification of these body tissue components in a production-mode, many clinical and research questions can be addressed objectively.

1.2 Related work

There are many methods available for body composition assessment[10]. Anthropometry is a non-invasive method which is easy to perform. Body mass index (BMI)[12], skin fold thickness[13,14], waist circumference, hip circumference, and waist-to-hip ratio[15] are the most common anthropometric measures used to assess body composition. However, these methods are based on the assumption that SAT has a constant relationship with whole-body adipose tissue. This assumption results in inaccuracy in the assessment of VAT and of measurement of adipose tissue in pathologic states. Even if the assumption is valid, it can achieve only rough estimation result. Bioelectrical impedance analysis (BIA) is an often-used method for estimating body composition, and in particular body fat. It is another non-invasive method with better accuracy than the anthropometry methods in healthy populations[10]. However, it assumes that the human body is a cylinder with equal conductance as well as stable hydration status, which may not be valid in patients with advanced disease conditions[16]. Consequently, BIA cannot overcome the influences of variations in different subjects that can lead to inaccurate measurement of body composition. Air displacement plethysmography (ADP) is also a non-invasive method based on the same principles as the reference standard method of hydrostatic weighing[17]. Although ADP is a recognized and scientifically validated densitometry method to measure human body composition, it still has some drawbacks. It has a strict requirement for the subject to fully exhale, which may be difficult to achieve in

This article is protected by copyright. All rights reserved.

Accepted Article

children and in patients with lung disease. ADP also cannot quantify the individual VAT and SAT components[10], let alone the individual non-fatty tissue components.

None of the above methods permits accurate regional quantification of body composition, and the fat quantification results may be unrelated to the amount of VAT[18]. Radiologic imaging techniques make the visualization and spatial localization of human internal structures possible, affording the potential for improving quantification accuracy. Dual-energy X-ray absorptiometry (DXA) is a reference standard method in body composition quantification because of its high precision and high stability for measurement[19]. However, DXA has a limited ability to distinguish between different compartments such as VAT and SAT[10]. Moreover, DXA is unnecessary for most disease conditions and requires additional radiation exposure if applied for body composition quantification. Unlike DXA, magnetic resonance imaging (MRI) and computed tomography (CT) images are routinely acquired in many clinical situations, and thus can be utilized to quantify body composition with little added healthcare cost. MRI can measure the quantity and distribution of body composition in the whole body without exposure to ionizing radiation, which makes it an ideal method for whole-body composition analysis. Yet, as it is more expensive, slower in terms of image acquisition time, and less widely available compared to CT[10,23], it has a more limited role in body-wide quantification of body composition. Moreover, it poses serious challenges to quantify bone tissues since they do not yield adequate MRI signals and are difficult to distinguish from other low signal intensity connective tissues such as ligaments and tendons. CT is widely used in body composition quantification[4,9,18,20] because it is easy to perform, has a short image acquisition time, and provides accurate, high-quality information on tissue composition in the body[21]. However, diagnostic CT is performed to scan only specific body regions depending on the clinical indication. Given its associated radiation dose, whole-body information is often not obtained and fully assessed.

This article is protected by copyright. All rights reserved.

Accepted Article

Until now, most body composition analysis methods based on CT have used single or multiple slices in a body region (mostly abdomen) to estimate the whole-body volume in any given individual[24-28]. Some investigators use the third lumbar vertebral region (L3) for analysis[24-26,45], others believe that the L4-L5 level is the best choice[27,28,46], and some others focus on using the slice or slices most correlated to whole-body volume[20,29]. Although use of a handful of slices may have strong correlation with the whole-body volume, use of these slices alone cannot accurately quantify body composition, since the distributions of body composition in different subjects are generally different, and high correlation does not imply high accuracy of prediction. There are also approaches to assess body composition based on a threshold method[30] as well as via manual operation[18,31]. However, the accuracy of thresholding is poor, and the manual operation method is labor-intensive, error-prone, and impractical when applied to the whole body or to a large number of imaging studies. Some methods aim at automatically segmenting adipose tissues, more specifically with a focus on separating SAT and VAT, from CT images[47-51]. The central idea of those methods is to seek the abdominal wall which separates SAT and VAT in the abdominal region. Many strategies, including curve smoothing[47], morphological operations[48], and mask matching[49-51], have been proposed to automatically achieve this objective. However, these methods cannot be applied to muscle and bone segmentation simultaneously with SAT/VAT segmentation/separation, and the performance is highly dependent on the accuracy of the location of the abdominal wall.

Positron emission tomography (PET)/computed tomography (CT), or PET/CT, provides co-registered molecular and anatomic images in a single imaging session, and is the most frequently used method for clinical molecular imaging assessment of patients with various disease conditions, most notably cancer[22,23]. The low-dose CT technique in PET/CT allows for a reduced radiation exposure, which facilitates whole-body CT imaging. Therefore,

This article is protected by copyright. All rights reserved.

Accepted Article

considering the above drawbacks of single-slice and body-region methods and the lack of availability of body-wide images, low-dose CT is an attractive modality for performing body composition analysis in certain disease conditions. Body composition analysis studies based on low-dose CT images are very few[34-36], and they are all limited in the level of automation achieved, the extent of body region covered, and the type of tissues considered. Pak et al[34] manually outline the volume of interest around the abdominal muscular wall and then uses thresholds to separate VAT on CT images. Adriana et al[36] calculate VAT and SAT volumes from L1 through L5 using semi-automated tracings. The above two methods require manual interaction on image slices of each target subject and do not segment bone and muscle tissues. Chan[35] presents a method which uses thresholds to evaluate the volume of lean body mass. However, the method is not yet tested on adipose tissues, let alone for separately quantifying VAT and SAT. A recent study presented by Hussein et al.[52] proposed a fully automatic method to segment SAT and VAT on low-dose CT images. They firstly utilized geometric median absolute deviation and local outlier scores to remove the outlier point. Then, sparse 3D conditional random fields algorithm was employed to achieve the segmentation. Although this method achieved superior assessment results for adipose tissue, it is applied only on the abdominal region, and muscle and bone tissues were not analyzed.

Given the challenges introduced by the suboptimal quality of low-dose CT images and the limitations of manual methods of segmentation including time-inefficiency, labor-intensiveness, and suboptimal accuracy and reproducibility, our goal in this paper is to develop a method of body composition analysis from low-dose CT images which are obtained as part of routine clinical PET/CT acquisition. Our approach adapts and substantially extends a recently developed methodology called Automatic Anatomy Recognition (AAR)[11] which is a general framework for the localization (called recognition) and delineation of multitudes of objects body-wide on CT, PET/CT, and MR images. It has

This article is protected by copyright. All rights reserved.

Accepted Article

been employed and tested in several medical image analysis applications, such as multi-organ recognition in whole-body PET/CT images[22], disease quantification in PET/CT images[40], auto-contouring organs at risk for radiation therapy planning[41], study of pediatric obstructive sleep apnea syndrome via MR images[42], and lymph node zone localization in PET/CT images[43]. Although our focus in this paper is not on multitudes of objects, we will exploit AAR's generic ability to accurately localize objects for supporting our method to delineate the tissue components of interest.

1.3 Outline of paper and approach

We will focus on the *body torso* (BT), defined to be the union of the thoracic, abdominal, and pelvic body regions. Our aim is to quantify four tissue components in BT – SAT, VAT, bone tissue, and muscle tissue – from low-dose CT images of given whole-body PET/CT acquisitions. Our method, which we will name *AAR-BCA* (BCA for *body composition analysis*) consists of three key steps – modeling BT with its ensemble of key objects from a population of patient images, recognition or localization of these objects in a given patient image *I*, and delineation and quantification of the four tissue components in *I* guided by the recognized objects. In the first step, a set of objects is first identified. The objects include anatomic organs and conceptual objects that are amenable to model and facilitate accurate recognition such as tissue regions and tissue interfaces. The latter are expressly formulated to facilitate the precise delineation of the four tissue components of our focus in BT. Modeling follows the principles of AAR of first precisely defining the anatomic extent of each object, generating binary delineations of the objects in the given image population following the definitions, determining the best hierarchical order in which the objects should be arranged for the specific application at hand, and constructing a *fuzzy anatomy model* of the object

This article is protected by copyright. All rights reserved.

Accepted Article

ensemble following the hierarchy[11]. The second step involves recognizing, or finding roughly the location of, each object in any given whole-body image *I* of a patient following the object hierarchy and guided by the built model. The third step makes use of this fuzzy localization information of the objects and the intensity distributions of the four tissue components, already learned and encoded in the model, to optimally delineate and quantify these components. Significant modifications and extensions engineered over the original AAR approach for arriving at AAR-BCA are fully described in Section 2 for each of the three steps. In Section 3, the experimental procedures involving whole-body PET/CT images from 38 subjects and the results are illustrated, and Section 4 summarizes our conclusions.

2. Materials and Methods

We will continue using the terminology of Udupa et al[11] but add some new notations that are specific to this work. Frequently used notations and their description are provided in Table 1 for convenience. Besides the body torso, we will also refer to the thoracic, abdominal, and pelvic body (sub) regions as body regions of interest in this paper.

The procedures of the AAR-BCA method are illustrated in Figure 1. They will be discussed in detail in the rest of Section 2.

2.1 Model building

As with previous AAR methodology[11], we start off by developing a precise anatomic definition of each object involved in the AAR-BCA process. Although our focus is the quantification of body composition in terms of subcutaneous adipose tissue (SAT), visceral adipose tissue (VAT), muscle (Msl), and skeleton (Sk) in BT, we will need additional objects to facilitate the accurate recognition and delineation of those objects of interest. These additional objects are listed in Table 2 along with their brief definitions, and are also

This article is protected by copyright. All rights reserved.

Accepted Article

illustrated on three axial slices (at the inferior, middle, and superior level for each object) on an *l*CT image of a representative patient in Figure 2. Although AAR is a generic methodology, it does not prescribe automatically methods of devising (including conceptual) objects and their hierarchy that is best suited for the application at hand.

It should be noted that although our final goal is BT-wide body composition quantification, the proposed method can also be applied to smaller regions of BT including the thorax (Thx), abdomen (Abd), and pelvis (Plv) as defined in Table 2.

We will first briefly summarize the AAR method[11], and then elaborate on our adaptations for the BCA application. The main idea behind AAR is to use the training data sets to build a fuzzy anatomy model of B. This model includes a fuzzy object-model for every object in B and the relationships between objects in B taken pairwise. The objects are arranged in a tree structure and the relationships between a parent and its children, which characterize the geographical layout of the objects relative to each other, are codified in the anatomy model. The intensity characteristics of each object are also estimated and included in the anatomy model. Then, using this anatomy model, in any given test image, every object in B is recognized or localized. The recognition result is a fuzzy mask for each object which determines the approximate position, shape, and size of the object.

Formally, the *fuzzy anatomy model* $FAM(B, G)$ is denoted by an ordered set of 5 entities $FAM(B, G) = (H, M, \rho, \lambda, \eta)$. The first entity H represents the hierarchy of objects, which is formed in a tree structure. $M = \{FM(O_\ell): \ell = 1, \ldots, L\}$ is a collection of object-models, one for each object. $\rho = \{\rho_k: k = 1, \ldots, L\}$ is a set of relationship measures where ρ_k denotes the relationship of object O_k with its unique parent. It contains information regarding the position as well as orientation relationship between O_k's parent and itself. The fourth parameter $\lambda = \{\lambda_k: k = 1, \ldots, L\}$is a set of scale ranges indicating the size range of each object O_k over the subject population. η denotes a set of measurements pertaining to the object assembly in B, which includes all of the necessary estimated measures in the AAR method such as object intensity characteristics. In particular, it includes the intensity distributions of the different objects which are needed for the optimal recognition and delineation of the objects.

This article is protected by copyright. All rights reserved.

The formulation of the objects to be considered, or equivalently, the choice of objects to be included in *H*, plays a vital role in the effective recognition and delineation of the specific tissue regions for the application at hand. Tissue regions SAT and VAT are both referred to as *sparse* objects[11], which are spatially sparse and not compact, and are usually significantly more challenging to model, recognize, and delineate compared to compact and blob-like objects. These objects, especially VAT, are highly variable over *G* and raise the question of their very modelability. To overcome these issues, we identify indirect or conceptual objects which do not pose these challenges, but which, once modeled and recognized, facilitate the precise delineation of the actual tissue regions of interest.

Following these ideas, in AAR-BCA we have identified two *indirect* or *conceptual* objects, denoted IAM and OBM as defined in Table 2, which play a pivotal role in the delineation and separation of SAT and VAT. As seen in Figure 2, OBM is defined as an object which is such that SAT is precisely the adipose (fat) tissue included within the object called Skin that is external to OBM (i.e., in the subcutaneous location). Similarly, IAM is formulated as an object which is such that VAT is exactly the adipose tissue that is inside of IAM (i.e., in the visceral location). In other words, if the position, shape, and size information of Skin, OBM, and IAM can be accurately obtained in a given image, SAT and VAT can be subsequently derived based on the intensity properties of adipose tissue and these three object masks using appropriate logical predicate functions. This is the central tenet of AAR-BCA. It is important to note that IAM and OBM are not real anatomic organs or objects, and, as is the case for many real anatomic objects, lack real tissue boundaries in several regions. For example, the posterior aspects of OBM and IAM inferiorly in the pelvis have no actual intervening tissue boundary between subcutaneous and visceral adipose tissue components as seen in Figure 2. We should emphasize that, in the thoracic region, the definition of and the separation between SAT and VAT is complicated because their precise boundaries are somewhat ambiguous. The reasons for this are that the dome of the diaphragm intersects slices in the mid and lower thoracic region, which brings portions of the abdominal visceral region into the thoracic slices, as well as the lack of an easily identifiable SAT-VAT interface in the region of the cervicothoracic junction.

This article is protected by copyright. All rights reserved.

Accepted Article

Figure 3 shows examples of hierarchies utilized in the AAR-BCA method for BT. Among these and many other hierarchies that have been tested, the one shown in Figure 3(a) has been found to be optimal from the perspective of object recognition, and hence, delineation. The main requirement for these hierarchies is that the root object should be easily recognizable. This is the reason that we chose the Skin object as the root. We will see later that although several objects listed in Table 2 are not explicitly entered in the selected hierarchy H, they all come into the picture in the AAR-BCA procedure eventually.

One other point of notation needs to be clarified. Although all objects in the set $\mathcal{O} = \{O_\ell: \ell = 1, \ldots, L\}$ as listed in Table 2 are of interest for AAR-BCA, not all objects will participate in every step. As we explained above, only the subset $\mathcal{O}_H = \{\text{Skin, Msl, IAM, OBM, Sk}\}$ will be involved in the model building and recognition processes. Another subset of objects $\mathcal{O}_{BC} = \{\text{SAT, VAT, Msl, Sk}\}$ will participate in the tissue quantification process. Furthermore, body regions {Thx, Abd, Plv} will enter into picture when we analyze the results of quantifying objects in $\mathcal{O}_{BC}$ confined to these body regions.

Given the set $\mathcal{I}$ of images, set $\mathcal{I}_\ell^b$ of binary images over $\mathcal{I}$ for each object O_ℓ considered in H, where each object is delineated as per the definitions in Table 2, and H itself, the process of constructing $FAM(B, G)$ follows the AAR methodology described in Udupa et al[11] in forming M, ρ, and λ. For the formation of the 5th entity η, however, the procedure is different in the actual information gathered while building $FAM(B, G)$. The way this information is used for delineation is also different which we will describe in Section 2.3. In the AAR approach[11], since delineation is performed by a model-based iterative relative fuzzy connectedness (IRFC) algorithm, the fuzzy affinity parameters needed by the IRFC algorithm for object O_ℓ are estimated from $\mathcal{I}_\ell^b$, other nearby co-object tissue regions, and $\mathcal{I}$. In AAR-BCA, the delineation procedure is different, as explained later, and requires just the intensity distribution within O_ℓ. This information is estimated as follows.

This article is protected by copyright. All rights reserved.

Accepted Article

Let $F_\ell(x)$ denote the intensity distribution of the tissue constituting object O_ℓ. We take $F_\ell(x)$ to be the image intensity histogram of the interior of O_ℓ over all samples of O_ℓ as represented in $\mathcal{I}$. To handle issues such as noise, missing intensities, artifacts due to segmentation, etc., instead of using $F_\ell(x)$ directly, we fit a smooth function to $F_\ell(x)$ and take the fit function as the intensity distribution for object O_ℓ. After observing $F_\ell(x)$ for objects $O_\ell \in \mathcal{O}_{BC}$, we decided to approximate $F_\ell(x)$ by the following function using a least squares method[37].

$$f_\ell(x)=a_1 e^{-\left(\frac{x-\mu_1}{\sigma_1}\right)^2}+a_2 e^{-\left(\frac{x-\mu_2}{\sigma_2}\right)^2} \quad (1)$$

All parameters of $f_\ell(x)$, including a_1, a_2, μ_1, μ_2, σ_1, and σ_2, are estimated using the Gauss-Newton method[38] to solve the nonlinear least squares problem. Figure 4 illustrates this fitting process for object Msl for our data set (see Section 3.1 for details on data set). The parameters of $f_\ell(x)$ for each object O_ℓ then become part of the entity η in $FAM(B, G)$. The intensity function $f_\ell(x)$ will be utilized in delineating the objects in $\mathcal{O}_{BC}$ as explained in Section 2.3. Notably, since the intensity distributions for objects SAT and VAT are the same, the fit intensity function $f_\ell(x)$ will also be the same for them. For bone tissue, a slightly modified half-version, namely $f_\ell^h(x)$, of $f_\ell(x)$ is used as the final membership function, where $f_\ell^h(x)$ is identical to $f_\ell(x)$ on the left shoulder of $f_\ell(x)$ up to the value of x where $f_\ell(x)$ reaches its maximum, and then $f_\ell^h(x)$ will remain at maximum value for all values of x. This is necessary to make sure that we capture soft and cortical bone tissue in the modified membership function $f_\ell^h(x)$.

This article is protected by copyright. All rights reserved.

Accepted Article

2.2 Object recognition

The purpose of recognition is to determine the pose, including position, rotation, and scale, of the object-model of a target object O_ℓ in a given test image I by using the anatomy model $FAM(B, G)$. The output $FM^T(O_\ell)$ of recognition is a transformed version of the fuzzy model $FM(O_\ell)$ of O_ℓ which indicates the location, orientation, and size of O_ℓ in I. Voxel-by-voxel it denotes the certainty of each voxel in $FM^T(O_\ell)$ to overlap with the actual object O_ℓ in I. The recognition procedure follows the hierarchy H chosen while building the model of B, and follows H top-down locating objects in I one by one. Firstly, the root object is recognized (see Udupa et al[11] for details). Then, while proceeding down H, assuming that the parent of O_ℓ is already recognized, the parent-offspring relationship ρ_ℓ is utilized to guide placement of O_ℓ relative to its parent in I. Subsequently, this pose is refined by an optimal search[11], which yields $FM^T(O_\ell)$. The main deviations here from the prior work[11] in the recognition procedure are: the body region BT is larger (compared to body regions neck, thorax, and abdomen dealt with separately in Udupa et al[11]), and the objects dealt with are different. Note that only the objects in $\mathcal{O}_H$ will be involved in recognition.

2.3 Object delineation

For any given image I, the recognition process yields a fuzzy mask $FM^T(O_\ell)$ over I for each object O_ℓ. We first utilize the intensity function $f_\ell(x)$ of O_ℓ to transform I into an intensity membership image, denoted $IM_\ell(I)$ which expresses at each voxel v of I the fuzzy membership of v in O_ℓ based only on the intensity characteristics of O_ℓ. We then delineate O_ℓ in I as a fuzzy membership image I_ℓ^D of O_ℓ by using a fuzzy predicate operation involving $FM^T(O_\ell)$ and $IM_\ell(I)$. With a slight extension of the notation, we denote the fuzzy membership

This article is protected by copyright. All rights reserved.

of $FM^T(O_\ell)$ at voxel v of I by $[FM^T(O_\ell)](v)$ and the intensity membership of $IM_\ell(I)$ at v by $[IM_\ell(I)](v)$. The latter is thus defined by $[IM_\ell(I)](v) = f_\ell(I(v))/C$, where C is a constant used for normalizing the membership values to [0, 1] range.

The basic idea of fuzzy delineation is to take the location information from the model component $FM^T(O_\ell)$ and the image intensity membership information from $IM_\ell(I)$ to decide on the final delineation membership $I_\ell^D(v)$ of each voxel v in I. In this process, for each object O_ℓ, two thresholds are employed, one Th_ℓ^{FM} for the fuzzy model membership value $[FM^T(O_\ell)](v)$ and another Th_ℓ^{IM} for the intensity membership value $[IM_\ell(I)](v)$ (see below as to how these thresholds are estimated automatically and optimally). The predicate operation is different for the different objects in $\mathcal{O}_{BC}$, as enumerated below.

For $O_\ell \in$ {Msl, Sk},

$$I_\ell^D(v) = \begin{cases} IM_\ell(v), & \text{if } \left[FM^T(O_\ell)\right](v) > Th_\ell^{FM} \ \&\ [IM_\ell(I)](v) > Th_\ell^{IM} \\ 0, & \text{otherwise} \end{cases}. \quad (2)$$

For O_ℓ = SAT,

$$I_\ell^D(v) = \begin{cases} IM_\ell(v), & \text{if } \left[FM^T(O_k)\right](v) < Th_\ell^{FM} \ \&\ [IM_\ell(I)](v) > Th_\ell^{IM} \\ 0, & \text{otherwise} \end{cases}, \text{ where } O_k = \text{OBM}. \quad (3)$$

For O_ℓ = VAT,

$$I_\ell^D(v) = \begin{cases} IM_\ell(v), & \text{if } \left[FM^T(O_k)\right](v) > Th_\ell^{FM} \ \&\ [IM_\ell(I)](v) > Th_\ell^{IM} \\ 0, & \text{otherwise} \end{cases}, \text{ where } O_k = \text{IAM}. \quad (4)$$

Note how objects IAM and OBM are utilized. The delineation of Msl and Sk (Equation (2)) is not influenced by IAM and OBM. The output membership at v is taken to be intensity membership $[IM_\ell(I)](v)$ if the model membership and the intensity membership both strongly

This article is protected by copyright. All rights reserved.

Accepted Article

confirm (above the respective thresholds) that v is to be considered to be in the object. Notably, the result itself is fuzzy. For SAT (Equation (3)), the exterior (complement) of the model FM^T(OBM) is taken as the model component of evidence, since SAT resides outside OBM (see Figure 2), and hence the logic shown in its predicate function. For VAT (Equation (4)), since it resides in the interior of object IAM (Figure 2), the logic is similar to those of Msl and Sk, with one difference, namely that the object used as model mask is IAM and not VAT itself.

Estimating optimal thresholds Th_ℓ^{FM} and Th_k^{IM}: We essentially perform a delineation rehearsal on the training image data set $\mathcal{I}$, and knowing the associated true delineations $\mathcal{I}_\ell^b$ for each object $O_\ell \in \mathcal{O}$, we estimate these thresholds by minimizing the delineation error. To elaborate, first the anatomy model $FAM(B, G)$ is built using $\mathcal{I}_\ell^b$, $\ell = 1, \ldots, L$, and $\mathcal{I}$. Then, the objects in $\mathcal{O}_H$ are recognized following the recognition methods, which yields, for each object O_ℓ in $\mathcal{O}_H$ and image I_n in $\mathcal{I}$, the fuzzy model $FM^T(O_\ell)$. Knowing the intensity function $f_\ell(x)$ of each object O_ℓ in $\mathcal{O}_{BC}$, we generate the intensity membership image $IM_\ell(I_n)$. Thus, for each image $I_n \in \mathcal{I}$, we now have $FM^T(O_\ell)$ for each $O_\ell \in \mathcal{O}_H$ and $IM_k(I_n)$ for each $O_k \in \mathcal{O}_{BC}$. Therefore, by using Equations (2)-(4), for any given thresholds t_1 on $FM^T(O_\ell)$ and t_2 on $IM_k(I_n)$, we can determine the delineations $I_k^D(v)$ for each $O_k \in \mathcal{O}_{BC}$ and $I_n \in \mathcal{I}$. Let the true delineation of O_k in I_n be $I_{n,k}^b$ (which is of course one of the images in the set $\mathcal{I}_k^b$) and let $Q_k(t_1, t_2)$ denote the sum of squares of the fuzzy false positive volume and fuzzy false negative volume[33] between $I_k^D(v)$ and $I_{n,k}^b$ over all images in $\mathcal{I}$. That is,

$$Q_k(t_1, t_2) = \sum_{I \in \mathcal{I}} \sum_{\text{all } v \text{ in } I} \left[(I_k^D(v) - I_{n,k}^b(v))^2 + (I_{n,k}^b(v) - I_k^D(v))^2 \right]. \quad (5)$$

Note here that $(I_k^D(v) - I_{n,k}^b(v))$ denotes the fuzzy false positive value at v. It is intended as a fuzzy logic operation (or fuzzy set difference) between the fuzzy membership image $I_k^D(v)$

This article is protected by copyright. All rights reserved.

and the binary image $I^b_{n,k}(v)$, meaning that the actual value $(I_k^D(v) - I^b_{n,k}(v))$ is taken only if it is positive; otherwise it is set to 0. The same principle applies to $(I^b_{n,k}(v) - I_k^D(v))$ which denotes the fuzzy false negative value at v. The optimal threshold pair (Th_ℓ^{FM}, Th_k^{IM}) is estimated by minimizing $Q_k(t_1, t_2)$.

$$\left(Th_\ell^{FM}, Th_k^{IM}\right) \in \underset{(t_1,\, t_2)}{\arg\min} \left[Q_k(t_1, t_2)\right]. \tag{6}$$

In our implementation, we use a multi-resolution strategy to search for optimal thresholds. From prior knowledge, we know the approximate range of values for these thresholds. The initial (coarse resolution) search is carried out based on this range and larger steps. Once an optimal pair is found, the search is refined using a smaller step size to search around and starting from the coarse optimal value. We set the coarse searching range of Th_ℓ^{FM} to the interval from the median value of $FM^T(O_\ell)$ to 1, and that of Th_k^{IM} to the interval from 0 to the median value of $IM_\ell(\mathcal{I})$. The step sizes of each iteration is $(0.1)^m$, where m denotes iteration number. Convergence is usually achieved within 3 to 4 iterations. Note that this step of finding optimal thresholds is actually performed in the model building stage, and (Th_ℓ^{FM},Th_k^{IM}) become part of item η of $FAM(B, G)$. We described this process under delineation for continuity of ideas and ease of reading.

After the delineation step, any small amounts of artifacts remaining in I_ℓ^D, caused by partial volume effects or residual components of the scanning table, etc., are suppressed by a 2D morphological opening operation performed in the slice plane for one iteration using a structuring element formed by the 8-neighbors of each pixel.

3. Experiments and Results

3.1 Image data sets

This retrospective study was conducted following approval from the Institutional Review Board at the Hospital of the University of Pennsylvania along with a Health Insurance Portability and Accountability Act waiver. The image data set used in our experiments was selected from our hospital patient image database by a board-certified radiologist (co-author

This article is protected by copyright. All rights reserved.

Accepted Article

DAT), and was verified to be of acceptable quality. This data set included 31 subjects with minimal focal abnormalities and 7 cancer patients. These subjects previously underwent ^{18}F-2-fluoro-2-deoxy-D-glucose (FDG) PET/CT imaging without administration of intravenous contrast material on a 16-detector row LYSO PET/CT scanner with time-of-flight capabilities (Gemini TF, Philips Healthcare, Bothell, WA). The low-dose CT images were acquired during quiet respiration using a kVp of 120, an effective mAs of 50, and a gantry rotation of time of 0.5 msec, and were reconstructed using a standard soft tissue kernel. For each subject, following the definition of BT (see Table 2), any extra slices falling outside the BT region were removed manually. Then, each of the 10 objects in the set $\mathcal{O}$ was segmented in each *l*CT image of the 38 PET/CT acquisitions to serve as the reference standard, adhering to the object definitions formulated in Table 2. The segmentation tools used include iterative live wire, thresholding, manual painting, and correction. The ground truth segmentations were performed by well-trained operators and verified for accuracy by the same radiologist. The data sets were from 25 male and 13 female subjects in the age range 31 – 83 years with BMI ranging from 17.27 to 38.28. The voxel sizes for CT and PET were, respectively, $1.2 \times 1.2 \times 4$ mm^3 and $4 \times 4 \times 4$ mm^3.

3.2 Evaluation methods and metrics

We employ a 5-fold cross validation strategy for evaluating AAR-BCA with a 25-13 train-test data set division. That is, the training set $\mathcal{I}$ consisting of 25 images is formed by randomly choosing 25 out of the 38 subjects, $FAM(B, G)$ is built based on these images, the performance of AAR-BCA is then tested on the images of the remaining 13 subjects, and the entire process is repeated 5 times for a total of 65 test cases. For each of the 5 test groups, normal subjects and cancer subjects appear in both training and testing data sets. Additionally, for any two groups, the number of overlapped subjects is no more than 20. The results reported are all based on 65 AAR-BCA experiments designed in this fashion.

Although our main focus is not object recognition in this paper, we will present its results, particularly for the hierarchies shown in Figure 3. As in the AAR approach[11], recognition accuracy is expressed by localization error and scale error. The former describes the distance of the geometric center of the actual object and the found model $FM^T(O_\ell)$ for each O_ℓ in $\mathcal{O}_H$.

This article is protected by copyright. All rights reserved.

Accepted Article

The latter denotes the ratio of the estimated object size to the true size. The ideal values for the two measures are 0 and 1, respectively.

For delineation, since our output is fuzzy (and not binarized), we will use false positive volume fraction (FPVF) and false negative volume fraction (FNVF) defined for comparing fuzzy delineations with binary ground truth delineations as formulated in Udupa et al.[33]. We have included a new metric based on Hausdorff boundary distance (HD) adapted to fuzzy delineations. We compute HD between a fuzzy output X_f and the corresponding binary true segmentation X_t by first thresholding X_f and then determining HD between the two binary volumes. HD will thus become a function of the chosen threshold. We will present the mean HD curve (as a function of the threshold on fuzzy membership) for each object in $\mathcal{O}_H$ computed over the 65 experiments to demonstrate how the boundary distance metric for the fuzzy delineation results varies for each delineated object.

3.3 Results

Sample recognition results for the hierarchy in Figure 3(a) are displayed in Figure 5 for one test image, where, for each object in $\mathcal{O}_H$, a slice of the fuzzy model $FM^T(O_\ell)$ at recognition is shown overlaid on the corresponding slice of the image. Table 3 lists the mean and standard deviation of location and size errors for the objects in $\mathcal{O}_H$ for the three hierarchies in Figure 3. As mentioned previously, the hierarchy in Figure 3(a) yielded the best recognition results among the hierarchies we tested, and so it is used subsequently for obtaining all delineation results. The reason it has the best recognition performance, we believe, is that Sk is encircled by Msl, and therefore it is more related to Msl than to other objects. Since Skin and IAM both surround Msl and in similar shape, the position and size errors of Msl are almost the same in all hierarchies.

Sample delineation results are displayed in Figure 6 for the objects in $\mathcal{O}_{BC}$ on one test image where the fuzzy delineations are overlaid on the original image slices. The ground truth delineations are also shown in a similar manner for comparison. Since the AAR-BCA results are fuzzy, depending on the membership at a voxel and due to translucent overlay, some

This article is protected by copyright. All rights reserved.

Accepted Article

subtle regions do not show up prominently, such as for VAT and SAT, although they are accurately delineated accounting for how such subtle and thin aspects will manifest themselves with somewhat different CT value (a bit brighter) than other "fat" fat regions due to partial volume effect.

Quantitative evaluations of AAR-BCA delineation results are summarized in Table 4 for the BT region for the four tissue types. The table also lists evaluation metrics by smaller body regions – for Thx, Abd, and Plv for the same tissues. Mean and standard deviation of FPVF and FNVF are listed for each object in $\mathcal{O}_{BC}$. Finally, Figure 7 portrays the boundary distance metric via mean HD curves obtained for the objects in $\mathcal{O}_{BC}$.

4. Discussion

For BT, over all objects, AAR-BCA achieves a FPVF of 3.7% and FNVF of 3.8%. Notably, SAT achieves a FPVF and FNVF both under 3%. For VAT, the FNVF of 4.8% is higher than for other objects, and so also for Msl (4.7%). VAT is a particularly challenging object to delineate since its total volume is small and it is spatially sparsely distributed within the body with a very complex shape as an object with subtle and thin aspects. This is exemplified by the inferior slice in the pelvic region for VAT in Figure 6. Because of these reasons, VAT segmentation is more challenging in the thorax and pelvis than in abdomen. Under these considerations, our result for VAT (as well as for SAT) is quite remarkable, especially in light of the lower quality of *l*CT images compared to diagnostic CT images. We believe this has been facilitated by the two conceptual objects we introduced into the AAR methodology, namely IAM and OBM, and also by the fuzzy stance taken for delineation. As we can see from Table 3, the recognition results for these objects are accurate enough to make the predicate functions perform their task of accurate delineations of SAT and VAT. This is a key central and novel idea underlying the AAR-BCA approach for body composition analysis.

The fuzzy boundary of AAR-BCA delineations cannot be strictly compared with the hard boundaries of the ground truth delineations. The novel boundary distance measure HD displayed in Figure 7 helps to some extent to illustrate how the iso-membership boundaries of AAR-BCA match the boundary of ground truth delineations. Note that, as can be expected, in

This article is protected by copyright. All rights reserved.

Accepted Article

closest match, the distance between the two boundaries is about 1 voxel (~4 mm). Object Sk demonstrates an interesting behavior where the match worsens at higher membership thresholds and again improves as this threshold is increased. We believe this is due to the fact that the ground truth delineations of bone actually contain two types of tissues – hard cortical bone and soft medullary bone. We believe that the accuracy for Sk would have been higher if we treated these two component tissues separately in ground truth delineations.

Note also that for Thx, Abd, and Plv, FPVFs and FNVFs mostly remain at the same level as for BT. In Thx, all objects achieve FPVFs under 5%, and SAT with FPVF < 3%. The FNVFs are a little higher than 4% for VAT, but under 4% for Sk and SAT. Msl has inferior FNVF, a little higher than 7%, in Thx compared to other regions. In Abd, Sk has the best results in both FPVF (2.6%) and FNVF (3.2%) among all body regions. However, Msl and VAT both have inferior FPVFs (both 6.6%) compared to other regions. In Plv, Msl has the best results in FPVF (4.2%) and FNVF (2.5%) among all regions. For the other three objects, the FPVFs are under 4% but FNVF ranges from 2.1% (for SAT) to 6.5% (for VAT). The above differences among different regions are mainly caused by the influence of other organs. In Thx and Abd for Msl, for example, confounding objects like stomach, large bowel, liver, etc. influence recognition as well as delineation.

The following computational times are estimated on a modern desktop Dell computer with the following specifications: 4-core Intel Xeon 3.3 GHz base to 3.7 GHz max turbo CPU with 8 GB RAM and running the GNU/Linux 3.11.10-25-desktop operating system. Building $FAM(B, G)$ from 25 *l*CT images using the hierarchy of Figure 3(a) takes about 3,410 seconds excluding the threshold optimization step of Equation (6) which takes about 4,600 seconds for all four objects. Thus, model building utilizing 23 cases takes about 2.2 hours in total. However, it should be emphasized that model building needs to be performed only once or very infrequently, and is thus really not a consideration of time cost. Moreover, this time cost is far less compared to atlas and deep learning techniques which can take many hours to days for training. Object recognition costs about 18 seconds per object per *l*CT image, and the actual delineation step costs less than 1 second per object per image. Thus, once the model $FAM(B, G)$ is built, full body torso composition analysis of the four tissue components can be completed fully automatically in about 1 minute per study.

This article is protected by copyright. All rights reserved.

Accepted Article

The related works described in Section 1.2 for body composition analysis usually need interactive operations, and many of them perform body composition analysis based on just one slice. Many of them focus on the problem of only quantifying SAT and VAT tissue components only and not muscle and bone and all 4 tissues silumtaneuously.

In our previous AAR work[11], we reported on the segmentation and quantification of SAT, VAT, and muscle in the abdomen (not the whole-body torso) and bone tissue in the thorax and abdomen utilizing contrast-enhanced diagnostic CT images. That approach modified an iterative relative fuzzy connectedness (IRFC) algorithm[32] to take model information for delineation following the object recognition step. It achieved (FPVF, FNVF) as follows for these tissue components. Abdominal SAT: (5%, 12%); abdominal muscle: (13%, 9%); abdominal skeleton: (6%, 14%); thoracic skeleton: (19%, 13%). Since that approach was based on modeling each object explicitly, and recognizing and then delineating the object, it did not directly delineate the VAT component since meaningful modeling of VAT is very difficult. AAR-BCA not only extends the body domain of application but also substantially improves on these earlier results through three key strategies: (1) Instead of modeling SAT and VAT objects directly, better "modelable" indirect objects are designed, defined anatomically in a consistent manner, and employed for delineating SAT and VAT tissue regions through them. (2) The collection of objects and their hierarchy within the AAR framework that best suits our goal of delineating the four tissue components is determined. (3) The IRFC algorithm is replaced by a logical predicate function involving the fuzzy models and intensity membership functions. While the model-based IRFC engine works well when solid organs are to be delineated as previously demonstrated[11], the sparse and scattered objects, particularly SAT, VAT, and Msl, pose challenges in accurately and automatically identifying an adequate set of seeds needed for their fuzzy connected delineation. Since it is difficult to ascertain that seeds are planted automatically in each scattered component of the same tissue region, the proposed fuzzy predicate solution works better than the previous AAR-IRFC.

In summary, AAR-BCA is able to handle other and more challenging body regions like the thorax and pelvis for efficient body composition analysis, even on *l*CT images, compared to currently existing solutions which mostly focus on the abdomen and only SAT and VAT. AAR-BCA performs simultaneous quantification of all 4 key tissue types, for which there is currently no demonstrated method in the literature.

This article is protected by copyright. All rights reserved.

Accepted Article

Accepted Article

5. Concluding Remarks

Motivated by applications in cancer and systemic diseases, our goal in this paper was to seek a practical method for body composition quantification which is automated, accurate, and efficient, and works on the region of the whole body (and not specialized to only a particular body region) where such analysis is needed, namely the body torso. Since PET/CT imaging is commonly used in the above disease conditions, we sought to perform body composition analysis on the more challenging *l*CT images that are acquired as part of routine PET/CT examination. Through a confluence of three key ideas – carefully designing the needed (including indirect) objects; finding the AAR hierarchy that is best suited for our application; and using a fuzzy predicate that combines model and intensity membership information – we extended the previous AAR approach to design the AAR-BCA method for quantifying bone tissue, muscle tissue, SAT, and VAT in the body torso. One important feature of AAR-BCA is that it is parameter free. All needed variables are automatically estimated from the training data sets, and no manual setting or adjustment of any parameters is needed. AAR-BCA can quantify the four tissue components in the body torso with under 5% overall error in about 1 minute per patient image.

In this work, we demonstrated the quantification results in body-torso-wide application, but also parcellated the results to smaller body regions to understand how accuracy varied over different body regions. AAR-BCA can also be applied to a smaller body region on diagnostic CT (*d*CT) or *l*CT. For instance, we can use abdominal *d*CT images for training and then quantify body composition on abdominal *d*CT images. We can also perform training on abdominal *l*CT images and then quantify on abdominal *d*CT images, or vice versa. Similar applications are feasible on MR images as well. For the intensity membership functions to make sense and to devise a proper predicate function, however, the MR images should first be corrected for intensity non-uniformity in each image and non-standardness over a population of subjects. Another future avenue is to use a fuzzy predicate function which is an appropriate direct parametric function of the two independent variables $[FM^T(O_\ell)](v)$ and $[IM_\ell(I)](v)$ in place of the functions in Equations (2)-(4). The parameters of such a function can be optimally estimated following the same approach described for estimating the two

This article is protected by copyright. All rights reserved.

thresholds. In fuzzy set theory[39], many membership functions are available which can be used as predicate functions.

The adoption of the recognition-delineation paradigm in AAR is by design and intentional and has several advantages as has been described in AAR publications. The AAR recognition operation is very robust to image variations as demonstrated in head and neck, thoracic, abdominal, and pelvic body regions on over 800 data sets and 80 objects in previous AAR publications[41, 43]. Image variations considered in those data sets were due to patient age, gender, and size, image acquisition parameters such as the use of a contrast agent, resolution, dose, reconstruction kernel, etc., and artifacts such as beam hardening artifacts, noise, body posture deviations, extent of pathology, etc. Employing a method to objectively score objects and images based on 9 quality criteria that are likely to influence segmentation, we observed[44] that, objects and images tend to group at the two ends of the quality score scale. In the task of delineating organs at risk for radiation therapy planning in head and neck and thoracic body regions, we have observed[41] that even when objects had poor quality score in the image, recognition was quite accurate although delineation was unable to perform at the same level of accuracy. If recognition is inaccurate, delineation is bound to be inaccurate. However, if recognition is accurate, delineation accuracy cannot be guaranteed. Streak artifacts arising from beam hardening are the worst offenders for recognition in particular and hence delineation as well in our experience with the above data sets considering variations commonly found in images. For AAR-BCA, we believe recognition accuracy will remain robust to image variations in this application as well and with an error within 1-3 voxels of object localization as reported in the paper. Delineation accuracy will be more susceptible to image variations. Since organs are much more heterogeneous in intensity properties, delineation of organs is much more challenging to make as robust as recognition compared to the tissue regions considered in this paper. This is because adiposity and muscle tissues are by definition homogeneous (at least more homogeneous) and therefore we believe that if recognition is robust for the application of this paper, delineation will be robust to image variations (at least some of them). Of course, this needs to be tested in the future with more extensive evaluations.

This article is protected by copyright. All rights reserved.

Accepted Article

One shortcoming of this current work is the small number of the image data sets utilized for evaluating performance. It would have been very useful to demonstrate this method's performance on 100s of data sets. A major challenge is the generation of ground truth segmentations, especially for adipose and muscle tissues, for adipose tissues because of their very complex shape, and for muscle due to the need for excluding subtle adipose pockets within muscle regions. Notably, bone ground truth segmentation has its own perils as well specially to include consistently the same trabecular bone components and to exclude similarly appearing parts from muscle tissues and voxels in the boundary between cortical bone and air influenced by partial volume effects. Ground truth generation is especially challenging in the thorax and pelvis. In the segmentation literature, the sample size we used is very common because of the above reason. Therefore, quite reasonably we decided to present these early results in this first paper. Another item of concern is how the accuracy of AAR-BCA may be affected by the presence of gross pathology. Although we included images with abnormalities in our study, this aspect needs to be studied more extensively.

Acknowledgements

The research reported in this paper is partly supported by the National Natural Science Foundation of China under grant no. 61802335; the Natural Science Foundation of Hebei Province of China under grant no. F2018203096; the China Postdoctoral Science Foundation under grant no. 2017M611188. Drs. Udupa and Torigian are the founders of a start-up company called Quantitative Radiology Solutions, LLC.

References

1. Nguyen T, Lau D C W. The Obesity Epidemic and Its Impact on Hypertension. *Can J Cardiol*. 2012; 28(3): 326-333.

2. Britton K A, Massaro J M, Murabito J M, Kreger B E, Hoffmann U, Fox C S. Body Fat Distribution, Incident Cardiovascular Disease, Cancer, and All-Cause Mortality. *J Am Coll Cardiol*. 2013; 62(10): 921-925.

This article is protected by copyright. All rights reserved.

Accepted Article

3. Kyrou I, Randeva H S, Weickert M O. Clinical Problems Caused by Obesity. In: De Groot L J, Beck-Peccoz P, Chrousos G, et al., editors. Endotext [Internet]. South Dartmouth (MA): MDText.com, Inc. 2000; Available from: http://europepmc.org/books/NBK278973

4. Baracos V E, Reiman T, Mourtzakis M, Gioulbasanis I, Antoun S. Body Composition in Patients with Non–Small Cell Lung Cancer: A Contemporary View of Cancer Cachexia with the Use of Computed Tomography Image Analysis. *Am J Clin Nutr*. 2010; 91(4): 1133S-1137S.

5. Fouladiun M, Körner U, Bosaeus I, Daneryd P, Hyltander A, Lundholm K G. Body Composition and Time Course Changes in Regional Distribution of Fat and Lean Tissue in Unselected Cancer Patients on Palliative Care—Correlations with Food Intake, Metabolism, Exercise Capacity, and Hormones. *Cancer*. 2005; 103(10): 2189-2198.

6. Erbil Y, Barbaros U, Sarı S, Agcaoglu O, Salmaslıoglu A, Ozarmagan S. The Effect of Retroperitoneal Fat Mass on Surgical Outcomes in Patients Performing Laparoscopic Adrenalectomy: the Effect of Fat Tissue in Adrenalectomy. *Surg Innov*. 2010; 17(2): 114-119.

7. Clark W, Siegel E M, Chen Y A, et al. Quantitative Measures of Visceral Adiposity and Body Mass Index in Predicting Rectal Cancer Outcomes After Neoadjuvant chemoradiation. *J Am Coll Surgeons*. 2013; 216(6): 1070-1081.

8. Singer J P, Peterson E R, Snyder M E, et al. Body Composition and Mortality After Adult Lung Transplantation in the United States. *Am J Resp Crit Care*. 2014; 190(9): 1012-1021.

9. Diaz A A, Zhou L, Young T P, et al. Chest CT Measures of Muscle and Adipose Tissue in COPD: Gender-based Differences in Content and in Relationships with Blood Biomarkers. *Acad Radiol*. 2014; 21(10): 1255-1261.

10. Di S K, Mourtzakis M. A Critical Evaluation of Body Composition Modalities Used to Assess Adipose and Skeletal Muscle Tissue in Cancer. *Appl Physiol Nutr Me*. 2012; 37(5): 811-821.

11. Udupa J K, Odhner D, Zhao L, et al. Body-Wide Hierarchical Fuzzy Modeling, Recognition, and Delineation of Anatomy in Medical Images. *Med Image Anal*. 2014; 18(5): 752-771.

This article is protected by copyright. All rights reserved.

Accepted Article

12. Organization W H. Obesity: Preventing and Managing the Global Epidemic. *World Health Organization Technical Report*. 1998; 894(1): 1-253.

13. Jackson A S, Pollock M L. Generalized Equations for Predicting Body Density of Men. *Brit J Nutr*. 1978; 40(3): 497-504.

14. Jackson A S, Pollock M L, Ward A. Generalized Equations for Predicting Body Density of Women. *Med Sci Sport Exer*. 1980; 12(3): 175-181.

15. Czernichow S, Kengne A P, Stamatakis E, Hamer M, Batty G D. Body Mass Index, Waist Circumference and Waist–Hip Ratio: Which is The Better Discriminator of Cardiovascular Disease Mortality Risk? Evidence from an Individual-Participant Meta-Analysis of 82864 Participants from Nine Cohort Studies. *Obes Rev*. 2011; 12(9): 680–687.

16. Kyle U G, Bosaeus I, De Lorenzo A D, et al. Bioelectrical Impedance Analysis—Part I: Review of Principles and Methods. *Clin Nutr*. 2004; 23(5): 1226-1243.

17. Mattsson S, Thomas B J. Development of Methods for Body Composition Studies. *Phys Med Biol* 2006; 51(13): 203-228.

18. Maurovich-Horvat P, Massaro J, Fox C S, Moselewski F, O'Donnell C J, Hoffmann U. Comparison of Anthropometric, Area- and Volume-Based Assessment of Abdominal Subcutaneous and Visceral Adipose Tissue Volumes Using Multi-Detector Computed Tomography. *Int J Obesity*. 2007; 31(3): 500-506.

19. Johnson J, Dawson-Hughes B. Precision and Stability of Dual-Energy X-ray Absorptiometry Measurements. *Calcified Tissue Int*. 1991; 49(3): 174-178.

20. Tong Y, Udupa J K, Torigian D A. Optimization of Abdominal Fat Quantification on CT Imaging Through Use of Standardized Anatomic Space: A Novel Approach. *Med Phys*. 2014; 41(6): 063501.

21. Gibson D J, Burden S T, Strauss B J, Todd C, Lal S. The Role of Computed Tomography in Evaluating Body Composition and the Influence of Reduced Muscle Mass on Clinical Outcome in Abdominal Malignancy: A Systematic Review. *Eur J Clin Nutr*. 2015; 69(10): 1079-1086.

22. Wang H, Udupa J K, Odhner D, Tong Y, Zhao L, Torigian D A. Automatic Anatomy Recognition in Whole-Body PET/CT Images. *Med Phys*. 2016; 43(1): 613-629.

This article is protected by copyright. All rights reserved.

Accepted Article

23. Martínez-Martínez F, Kybic J, Lambert L, Mecková Z. Fully Automated Classification of Bone Marrow Infiltration in Low-Dose CT of Patients with Multiple Myeloma Based on Probabilistic Density Model and Supervised Learning. *Comput Biol Med*. 2016; 71(C): 57-66.

24. Sebastiano K M D, Yang L, Zbuk K, et al. Accelerated Muscle and Adipose Tissue Loss May Predict Survival in Pancreatic Cancer Patients: the Relationship with Diabetes and Anaemia. *Brit J Nutr*. 2013; 109(2): 302-312.

25. Martin L, Birdsell L, Macdonald N, et al. Cancer Cachexia in the Age of Obesity: Skeletal Muscle Depletion is A Powerful Prognostic Factor, Independent of Body Mass Index. *J Clin Oncol*. 2013; 31(12): 1539-1547.

26. Antoun S. Sarcopenia Is Linked to Treatment Toxicity in Patients with Metastatic Colorectal Cancer. *Nutr Cancer*. 2014; 66(4): 583-589.

27. Anderson P J, Chan J C, Chan Y L, et al. Visceral Fat and Cardiovascular Risk Factors in Chinese NIDDM Patients. *Diabetes Care*. 1997; 20(20): 1854-1858.

28. Goodpaster B H, Kelley D E, Wing R R, Thaete F L. Effects of Weight Loss on Regional Fat Distribution and Insulin Sensitivity in Obesity. *Diabetes*. 1999; 48(4): 839-847.

29. Shen W, Punyanitya M, Wang Z, et al. Total Body Skeletal Muscle and Adipose Tissue Volumes: Estimation from A Single Abdominal Cross-Sectional Image. *J Appl Physiol*. 2004; 97(6): 2333-2338.

30. Goodpaster B H, Thaete F L, Kelley D E. Composition of Skeletal Muscle Evaluated with Computed Tomography. *Ann Ny Acad Sci*. 2000; 904(1): 18-24.

31. Fox C S, Massaro J M, Hoffmann U, et al. Abdominal Visceral and Subcutaneous Adipose Tissue Compartments: Association with Metabolic Risk Factors in the Framingham Heart Study. *Circulation*. 2007; 116(1): 39-48.

32. Ciesielski K C, Udupa J K, Falcão A X, Miranda P A V. Fuzzy Connectedness Image Segmentation in Graph Cut Formulation: A Linear-Time Algorithm and a Comparative Analysis. *J Math Imaging Vis*. 2012; 44(3): 375-398.

33. Udupa J K, Leblanc V R, Ying Z, et al. A Framework for Evaluating Image Segmentation Algorithms. *Comput Med Imag Grap*. 2006; 30(2): 75-87.

34. Pak K, Lee S H, Lee J G, Seok J W, Kim I J. Comparison of Visceral Fat Measures with Cardiometabolic Risk Factors in Healthy Adults. *Plos One*. 2016; 11(4): 1-10.

This article is protected by copyright. All rights reserved.

Accepted Article

35. Chan T. Computerized Method for Automatic Evaluation of Lean Body Mass from PET/CT: Comparison with Predictive Equations. *J Nucl Med*. 2012; 53(1): 130-137.

36. Oliveira A L, Azevedo D C, Bredella M A, Stanley T L, Torriani M. Visceral and Subcutaneous Adipose Tissue FDG Uptake by PET/CT in Metabolically Healthy Obese Subjects. *Obesity*. 2015; 23(2): 286–289.

37. Stigler S M. Gauss and the Invention of Least Squares. *Ann Stat*. 1981; 9(3): 465-474.

38. Gratton S, Lawless A S, Nichols N K. Approximate Gauss–Newton Methods for Nonlinear Least Squares Problems. *Siam J Optimiz*. 2007; 18(1): 106-132.

39. Kaufmann A. *Introduction to the Theory of Fuzzy Subsets, Volume I, Fundamental Theoretical Elements*. New York, Academic Press Inc.; 1975.

40. Tong Y, Udupa JK, Odhner D, Wu C, Schuster SJ, Torigian DA. Disease Quantification in PET/CT Images without Explicit Object Delineation, *Medical Image Analysis*, https://doi.org/10.1016/j.media.2018.11.002, 2018.

41. Wu X, Udupa JK, Tong Y, Odhner D, Pednekar GV, Simone II CB, McLaughlin DJ, Apinorasethkul C, Lukens J, Mihailidis D, Shammo G, James P, Camaratta J, Torigian DA. Auto-contouring via Automatic Anatomy Recognition of Organs at Risk in Head and Neck Cancer on CT images, *Proceedings of SPIE*, 10576: 1057617-1 – 1057617-7, 2018.

42. Xu G, Udupa JK, Tong Y, Cao H, Odhner D, Torigian DA, Wu X. Thoracic lymph node station recognition on CT images based on automatic anatomy recognition with an optimal parent strategy, *Proceedings of SPIE*, 10574: 10574F-1 – 10574F7, 2018.

43. Tong Y, Udupa J K, Odhner D, et al. Automatic anatomy recognition in post-tonsillectomy MR images of obese children with OSAS. *Proceedings of SPIE*, 9414: 94140Z-1 - 94140Z-6, 2015.

44. Pednekar GV, Udupa JK, McLaughlin DJ, Wu X, Tong Y, Simone II CB, Camaratta J, Torigian DA. Image Quality and Segmentation, *Proceedings of SPIE*, 10576: 105762N-1 - 105762N-7, 2018.

45. H. Chung, D. Cobzas, L. Birdsell, J. Lieffers, and V. Baracos. Automated segmentation of muscle and adipose tissue on CT images for human body composition analysis, *Proceedings of SPIE*, 7261: 72610K, 2009.

This article is protected by copyright. All rights reserved.

Accepted Article

46. Pednekar A, Bandekar A N, Naghavi M, et al. Automatic Segmentation of Abdominal Fat from CT Data, *IEEE Workshops on Application of Computer Vision*, 308-315, 2005.

47. Zhao B, Colville J J, Curran S, et al. Automated quantification of body fat distribution on volumetric computed tomography. *J Comput Assist Tomogr*, 2006, 30(5): 777-783.

48. Mensink S D, Spliethoff J W, Belder R, et al. Development of automated quantification of visceral and subcutaneous adipose tissue volumes from abdominal CT scans, *Proceedings of SPIE*, 7963: 79632Q, 2011.

49. Kim Y J, Lee S H, Kim T Y, et al. Body fat assessment method using CT images with separation mask algorithm. *J Digit Imaging*, 2013, 26(2): 155-162.

50. Kim Y J, Park J W, Kim J W, et al. Computerized automated quantification of subcutaneous and visceral adipose tissue from computed tomography scans: development and validation study. *JMIR Med Inform*, 2016, 4(1): e2.

51. Romero D, Ramirez J C, Mármol A. Quanification of subcutaneous and visceral adipose tissue using CT, *IEEE International Workshop on Medical Measurement and Applications*, 128-133, 2006.

52. Hussein S, Green A, Watane A, et al. Automatic segmentation and quantification of white and brown adipose tissues from PET/CT scans. *IEEE T Med Imaging*, 2017, 36(3): 734-744.

Accepted Article

This article is protected by copyright. All rights reserved.

Figure Legends

Figure 1	A schematic representation of the AAR-BCA approach.
Figure 2	Some representative examples of objects considered in AAR-BCA. The green masks superimposed on the *l*CT images are manually segmented object regions. Each row, from left to right, shows three axial slices selected from the inferior, middle, and superior aspects of the body torso in the same subject. See Table 2 for definition of the objects.
Figure 3	Examples of hierarchies tested in AAR-BCA.
Figure 4	Left: Intensity histogram $F_\ell(x)$ for Msl. Right: The fit function $f_\ell(x)$ together with $F_\ell(x)$.
Figure 5	Sample recognition results on a test image for objects in the hierarchy in Figure 3(a). Top-down: Three slices selected from superior, middle, and inferior aspects of the body torso are shown, with original slices in the first column, and slices of recognized objects overlaid on original slices in other columns.
Figure 6	Sample delineation results for AAR-BCA. For each object delineated, the fuzzy delineation (lower row) and ground truth delineation (upper row) are shown overlaid on the original test image slices. Slices selected from inferior (left), middle (middle), and superior (right) aspects of each object are shown.
Figure 7	Illustration of delineation accuracy via fuzzy boundary distance curves. The mean HD curves for the delineations of SAT, Msl, Sk, and VAT produced by AAR-BCA over all experiments are displayed.

Accepted Article

This article is protected by copyright. All rights reserved.

Table 1. Definitions of notations utilized in AAR-BCA

Notations	Definition
BT	Body torso consisting of thorax, abdomen, and pelvis.
B	Body region of interest which by default is BT in this paper.
G	Human population group under consideration for both training parameters and testing.
*l*CT	Low-dose CT images in a PET/CT acquisition.
$\mathcal{I} = \{I_1, \ldots, I_N\}$	The set of *l*CT images of B of human subjects who belong to G.
$\mathcal{O} = \{O_1, \ldots, O_L\}$	L objects considered in B for the AAR-BCA procedure.
$\mathcal{I}_\ell^b = \{I_{1,\ell}, \ldots, I_{N,\ell}\}$	The set of binary images representing the true delineations of object O_ℓ in the images in $\mathcal{I}$.
$FM(O_\ell)$	Fuzzy model of O_ℓ derived by AAR.
$FAM(B, G)$	Fuzzy anatomy model of the whole object assembly in B for a specified hierarchical arrangement of the objects, derived from all ground truth images in $\mathcal{I}_\ell^b$.
$FM^T(O_\ell)$	Fuzzy model $FM(O_\ell)$ of object O_ℓ after it has been transformed to match O_ℓ optimally in a given test image I.
$F_\ell(x)$	Histogram of the tissue constituting object O_ℓ within population G.
$f_\ell(x)$	Parametric intensity function fit to $F_\ell(x)$.
$IM_\ell(I)$	Intensity membership image of I in O_ℓ based only on $f_\ell(x)$.
I	A given test *l*CT image.
I_ℓ^D	Fuzzy delineation of O_ℓ in a given test image I expressed as an image.

This article is protected by copyright. All rights reserved.

Table 2. Definitions of body regions and objects in the body torso.

Abbreviation	Definition
Thx	Thoracic region extending from 5 mm inferior to the bases of the lungs to 15 mm superior to the lung apices.
Abd	Abdominal region extending from the point of bifurcation of the abdominal aorta into common iliac arteries to the superior aspect of the liver.
Plv	Pelvic region extending from the inferior aspect of the ischial tuberosities to the point of bifurcation of the abdominal aorta into common iliac arteries.
BT	Body torso extending from the inferior aspect of the pelvic region to the superior aspect of the thoracic region.
Skin	The outer boundary of the skin (arms excluded) in the body torso. The interior region constitutes the entire body torso region.
Msl	All skeletal musculature in the body torso region.
Sk	All skeletal structures in the body torso region.
SAT	Subcutaneous adipose tissue in the body torso region.
VAT	Visceral adipose tissue (internal to Msl) in the body torso region.
IAM	The inner aspect of Msl. The interior region includes all visceral organs in the body torso, such as liver, lungs, etc., as well as air, fluid, and VAT in the body torso region.
OBM	The outer boundary of Msl. The interior region includes Msl, Sk, and IAM.

Accepted Article

This article is protected by copyright. All rights reserved.

Table 3. Location error (in mm) and size error for the hierarchies shown in Figure 3. Mean and standard deviation (in parenthesis) values are listed in each cell.

	Hierarchy a		Hierarchy b		Hierarchy c	
	Loc error (mm)	Size error	Loc error (mm)	Size error	Loc error (mm)	Size error
Skin	7.6 (4.6)	1.00 (0.01)	7.6 (4.6)	1.00 (0.01)	7.6 (4.6)	1.00 (0.01)
Msl	11.0 (6.9)	0.99 (0.03)	11.0 (6.9)	0.99 (0.03)	11.1 (7.1)	0.99 (0.02)
Sk	12.2 (5.7)	0.97 (0.03)	13.6 (6.8)	0.96 (0.03)	13.8 (7.2)	0.96 (0.03)
IAM	16.0 (7.0)	1.06 (0.03)	16.0 (7.0)	1.06 (0.03)	16.0 (7.0)	1.06 (0.03)
OBM	7.1 (4.2)	1.00 (0.02)	7.1 (4.2)	1.00 (0.02)	7.1 (4.2)	1.00 (0.02)

Accepted Article

This article is protected by copyright. All rights reserved.

Table 4. The mean and standard deviation of fuzzy FPVF and FNVF of the AAR-BCA delineations for BT, Thx, Abd, and Plv body regions.

	BT		Thx		Abd		Plv	
	FPVF	FNVF	FPVF	FNVF	FPVF	FNVF	FPVF	FNVF
SAT	0.029	0.024	0.022	0.036	0.032	0.026	0.030	0.021
	0.021	0.026	0.014	0.049	0.029	0.037	0.020	0.026
Msl	0.047	0.047	0.043	0.071	0.066	0.058	0.042	0.025
	0.018	0.057	0.017	0.062	0.027	0.064	0.021	0.038
Sk	0.031	0.034	0.032	0.037	0.026	0.032	0.035	0.035
	0.016	0.035	0.017	0.044	0.014	0.040	0.019	0.034
VAT	0.042	0.048	0.031	0.045	0.066	0.036	0.033	0.065
	0.026	0.037	0.030	0.034	0.045	0.025	0.017	0.061

Accepted Article

This article is protected by copyright. All rights reserved.

Accepted Article

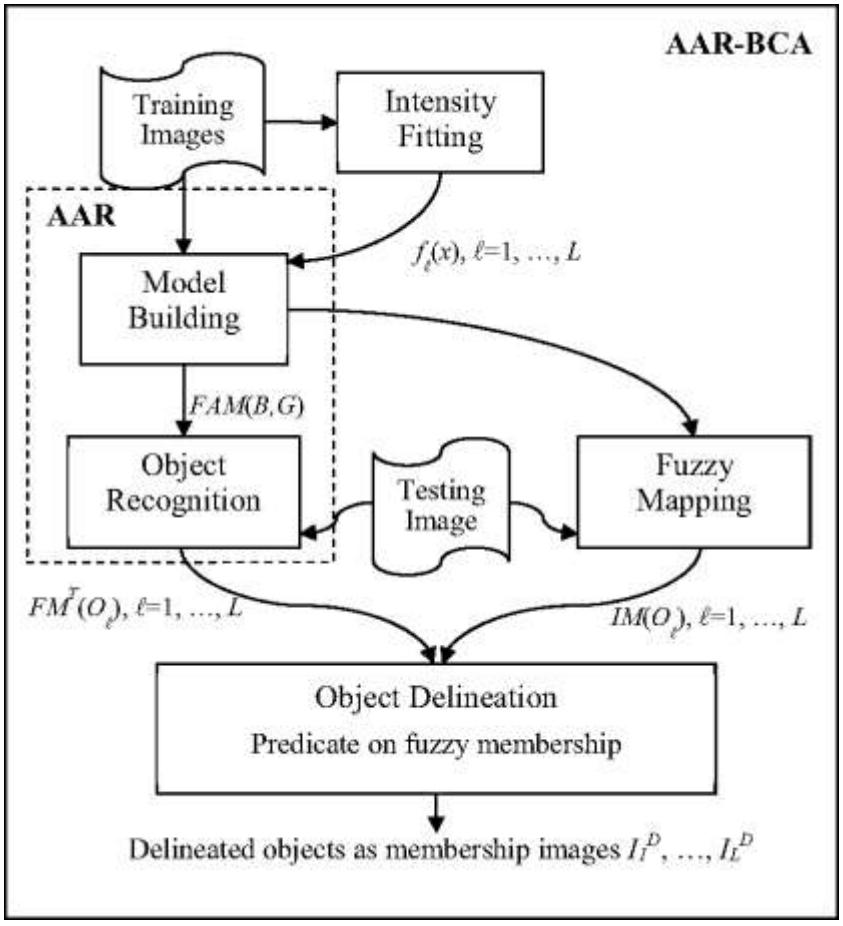

This article is protected by copyright. All rights reserved.

Accepted Article

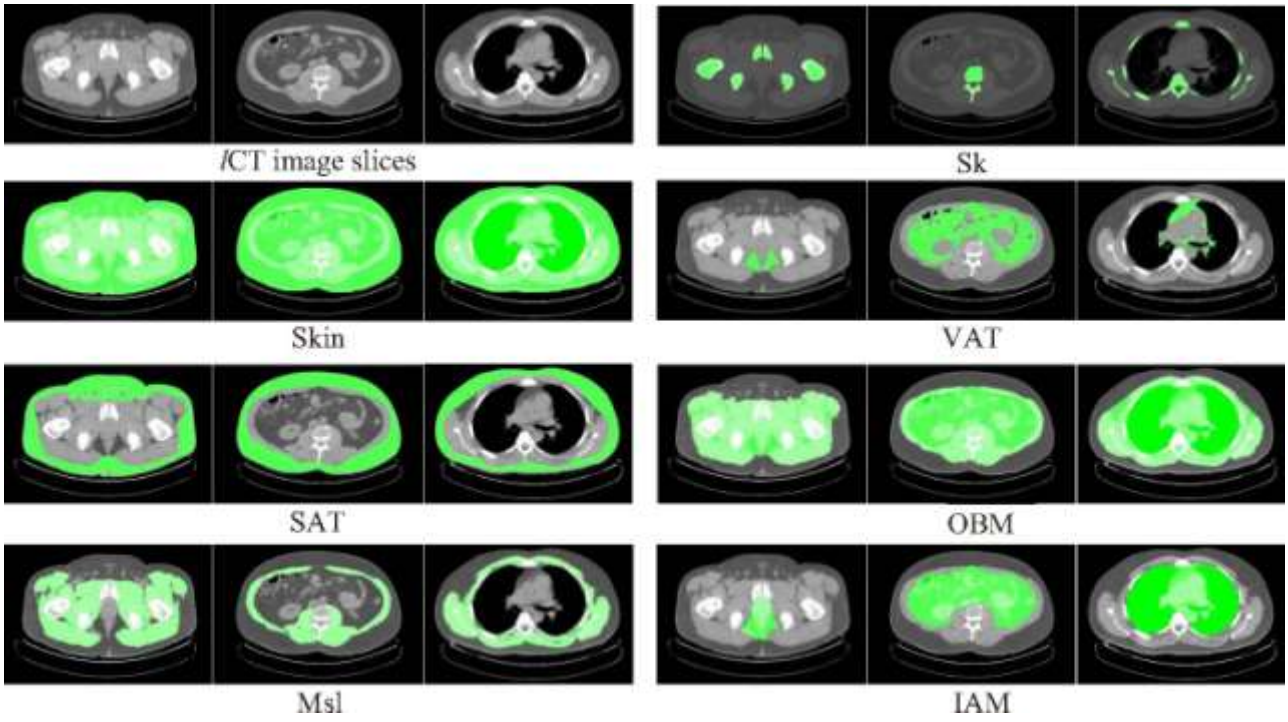

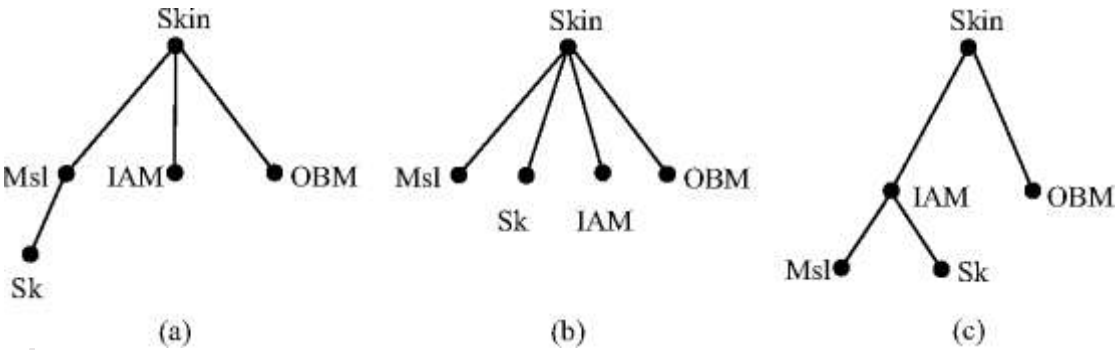

This article is protected by copyright. All rights reserved.

Accepted Article

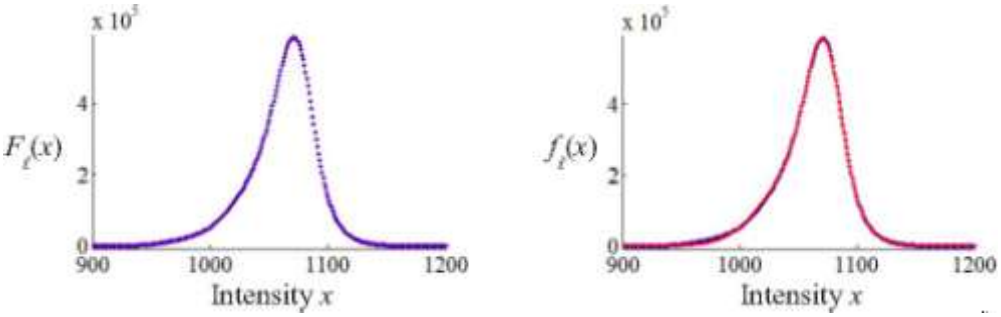

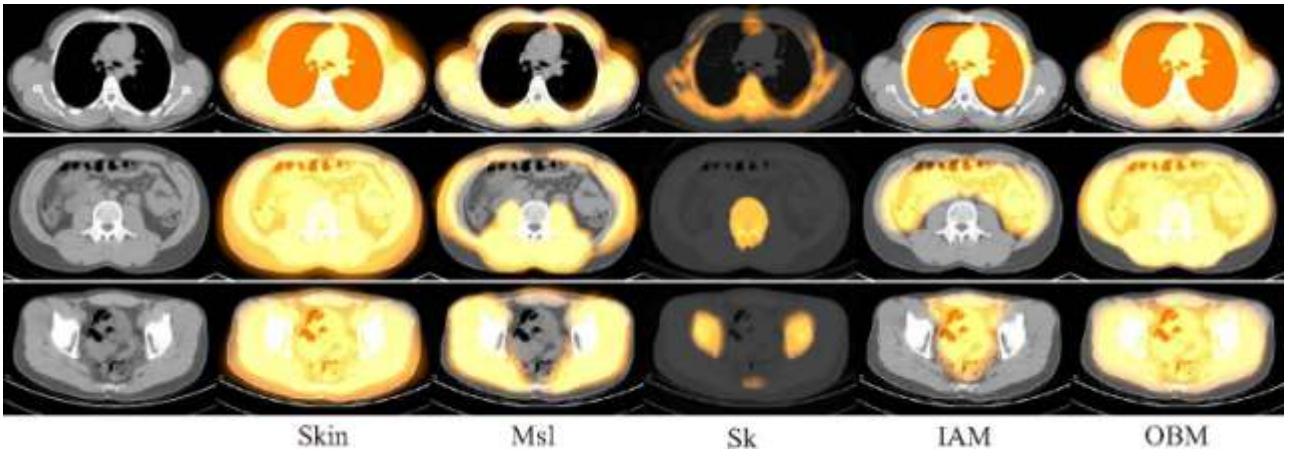

This article is protected by copyright. All rights reserved.

Accepted Article

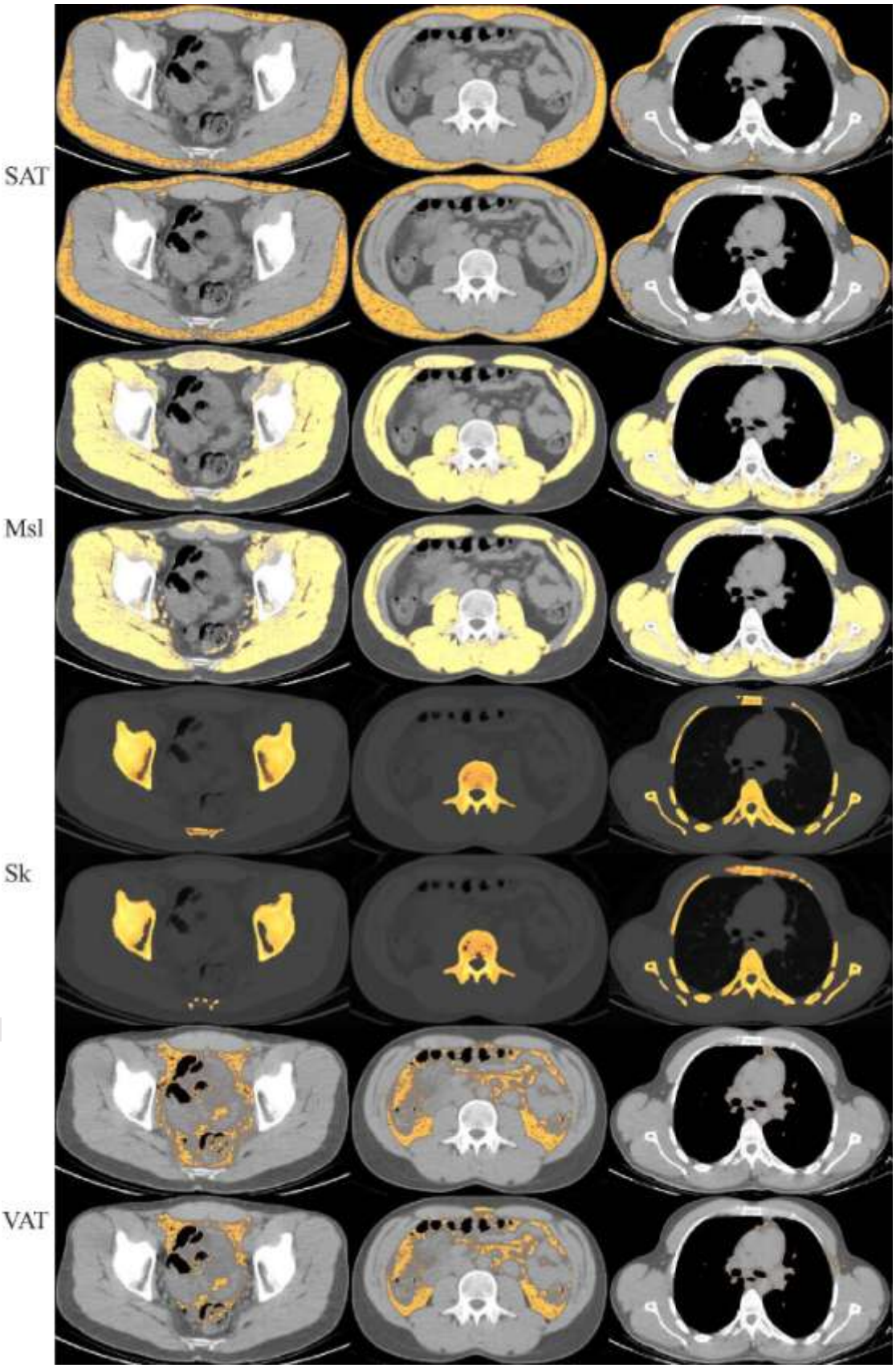

This article is protected by copyright. All rights reserved.

Accepted Article

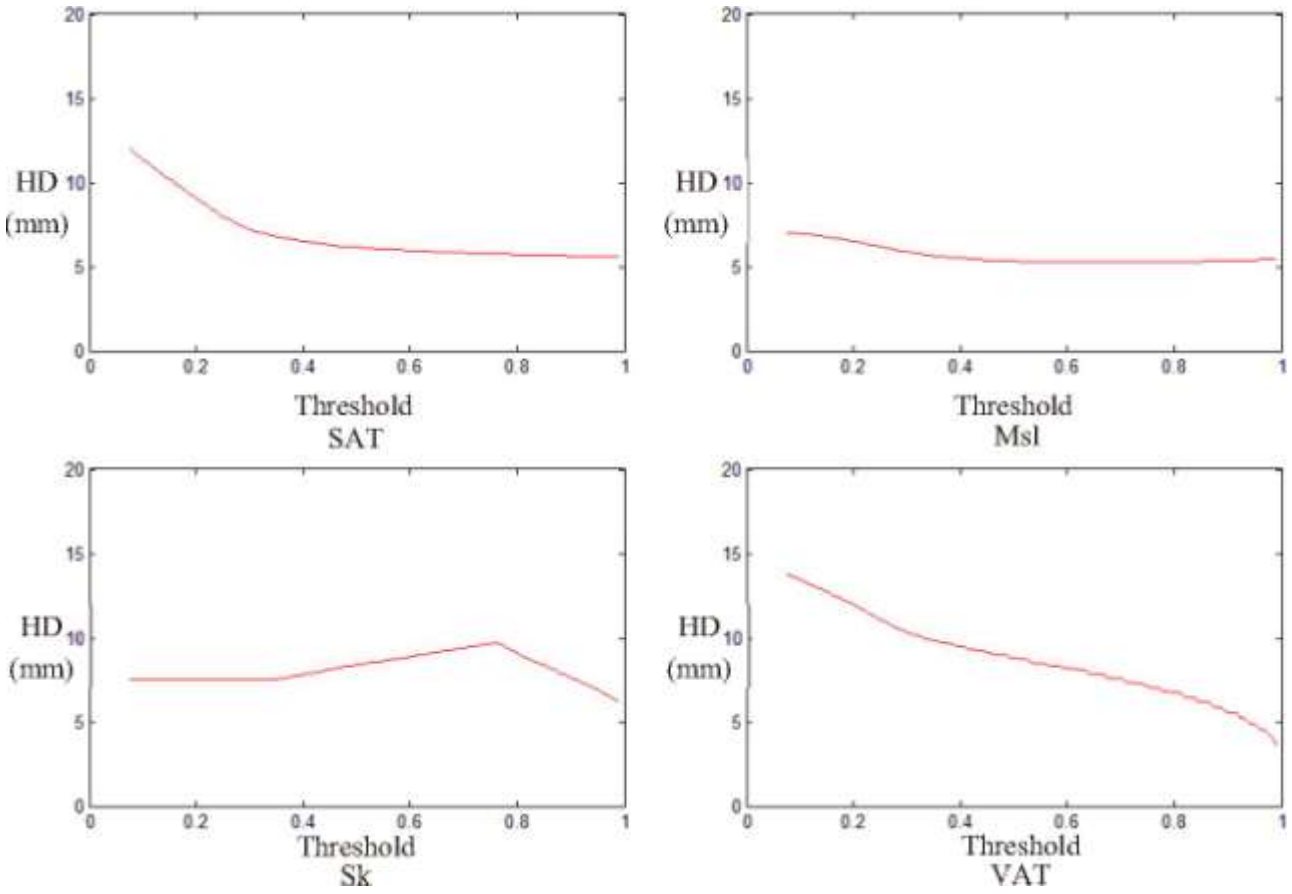

This article is protected by copyright. All rights reserved.